Hybrid model based unified scheme for endoscopic Cerenkov and radio-luminescence tomography: simulation demonstration

Lin Wang[1], Xin Cao[1], Qingyun Ren[1], Xueli Chen[2,a)], Xiaowei He[1,a)]
[1]School of Information Sciences and Technology, Northwest University, Xi'an, Shaanxi 710127, China
[2]School of Life Science and Technology, Xidian University, Xi'an, Shaanxi 710126, China

Abstract:
Cerenkov luminescence imaging (CLI) is an imaging method that uses an optical imaging scheme to probe a radioactive tracer. Application of CLI with clinically approved radioactive tracers has opened an opportunity for translating optical imaging from preclinical to clinical applications. Such translation was further improved by developing an endoscopic CLI system. However, two-dimensional endoscopic imaging cannot identify accurate depth and obtain quantitative information. Here, we present an imaging scheme to retrieve the depth and quantitative information from endoscopic Cerenkov luminescence tomography (endoscopic CLT), which can also be applied for endoscopic radio-luminescence tomography (endoscopic RLT). In the scheme, we first constructed a physical model for image collection, and then a mathematical model for characterizing the luminescent light propagation from tracer to the endoscopic detector. The mathematical model is a hybrid light transport model combined with the 3rd order simplified spherical harmonics approximation, diffusion, and radiosity equations to warrant accuracy and speed. The mathematical model integrates finite element discretization, regularization, and primal-dual interior-point optimization to retrieve the depth and the quantitative information of the tracer. A heterogeneous-geometry-based numerical simulation was used to explore the feasibility of the unified scheme, which demonstrated that it can provide a satisfactory balance between imaging accuracy and computational burden.

a) Author to whom correspondence should be addressed: xlchen@xidian.edu.cn, hexw@nwe.edu.cn

This manuscript was accepted by J. Appl. Phys. Click here to see the version of record.

1. Introduction

Cerenkov luminescence imaging (CLI) has emerged as a new molecular imaging modality in recent years, and its potential application to a wide range of areas has attracted the interest of many scientists.[1-4] By using an optical imaging scheme to probe a clinically approved radioactive tracer, CLI has opened an opportunity for translating optical imaging from preclinical to clinical applications. For example, it has been clinically used for detecting Cerenkov radiation emitted from the thyroid gland in a patient treated for hyperthyroidism,[5] for detecting nodal disease in patients undergoing diagnostic ^{18}F-FDG scans,[6] and for intraoperatively assessing the tumor's resection margins in breast-conserving surgery.[7] However, in all the cases imaging is focused on the superficial lesions due to the limited penetration depth of the Cerenkov luminescent light. To image deep lesions, an endoscopic system for CLI has been developed,[8-11] and effectively applied to detect and quantify features associated with gastrointestinal disease.[11] Due to the low signal level of Cerenkov luminescence, long acquisition time is usually required to obtain a reasonable endoscopic CLI image (several minutes in [11]). Fortunately, several strategies can be applied to accelerate the acquisition speed, such as by improving the imaging system, by using new imaging methods,[12,13] or by using radioluminescent nanoparticles (RLNP).[14-17] With the help of RLNP, endoscopic radioluminescence imaging (endoscopic RLI), a type of sensitivity-improved endoscopic CLI, was developed to improve the sensitivity of endoscopic CLI by 50-fold.[18] Thus, an image can be acquired within several seconds, which enhances the *in vivo* applicability of the endoscopic CLI system. Although the endoscopic CLI or RLI system has great potential in detecting and recognizing pathologic regions, the two-dimensional images produced by this system cannot identify the accurate depth of the light source and obtain the related quantitative information. Therefore three-dimensional (3D) tomographic technique is needed for endoscopic CLI or RLI.

Piao et al. first performed endoscopic optical tomography (EOT) in 2006.[19] The authors proposed an endoscopic geometry and accordingly designed an instrument. Subsequently, Chen et al. developed a more realistic endoscopic geometry and a reliable endoscopic algorithm.[20,21] In their work, they used a hybrid diffusion approximation and radiosity theory based light transport model and incorporated the aperture angle of the objective to construct the imaging geometry. Gao et al. have also developed image reconstruction algorithms for fluorescence based EOT in frequency domain.[22,23] All the published EOT geometry models are based on diffusion approximation (DA). Both the Cerenkov and radio-luminescence spectra cover wavelengths from 400 to 900 nm,[1,2,15,16] hence most of the energy detected by CLI is distributed at the lower wavelength range of the device response spectrum (<500 nm for CL, and 550-750 nm for radioluminescence). We calculated the optical properties of the commonly used tissues in a mouse model, including the absorption and reduced scattering coefficients,[24] as shown in Fig. 1(a) and 1(b) respectively. We found that the absorption is dominant over the scattering effect in the low wavelength range for most tissues, which could also be seen from the ratio of the reduced scattering coefficient over the absorption [Fig. 1(c)]. In such case, the DA cannot accurately describe the light propagation process because the highly diffuse assumption fails,[25] thus, the DA based EOT geometries are not applicable to endoscopic CLT and RLT. To address this problem, here we present a hybrid-light-transport-model-based unified scheme for endoscopic CLT and RLT. In the scheme, we first constructed a physical model for image collection, and then a mathematical model to describe luminescent light propagation from the tracer to the endoscopic detector. The mathematical model is a hybrid light transport model combined with the 3rd order simplified spherical harmonics approximation (SP_3), diffusion, and radiosity equations to warrant accuracy and speed. By integrating finite element discretization and regularization strategy, the mathematical model was solved with primal-dual interior-point optimization to retrieve the depth and quantitative information of the tracer. Finally, the

feasibility of the unified scheme was evaluated by a heterogeneous-geometry-based numerical simulation.

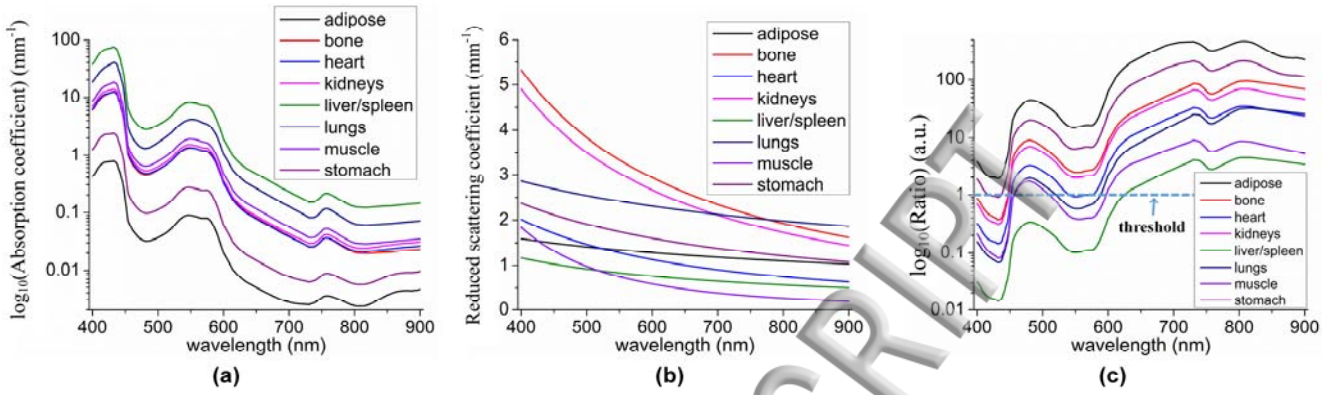

Fig. 1 Optical properties of the commonly used tissues in a mouse model between the wavelengths of 400 to 900 nm. (a) Absorption coefficient; (b) Reduced scattering coefficient; and (c) Ratio of the reduced scattering coefficient to the absorption coefficient.

2. Methods

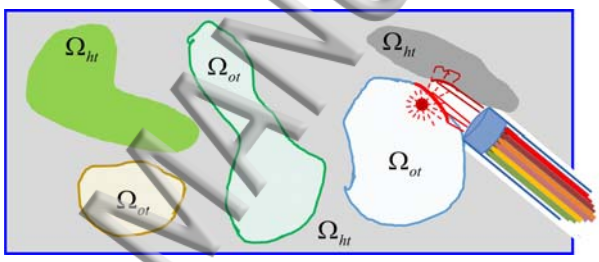

Fig. 2 The concept of the hybrid light transport model based endoscopic CLT/RLT geometry.

Figure 2 illustrates the concept of the hybrid light transport model based endoscopic geometry and the principle of the endoscopic detection scheme. In Fig. 2, Ω_{ht} denotes the region of the high-scattering tissue. Ω_{ot} shows the region of other scattering tissue, here the other scattering tissue includes the low-scattering tissue, the high absorption tissue, and the source located region. During endoscopic imaging, the Cerenkov or radio-luminescent light first propagates in tissues (including both the high- and other scattering tissues), then transfers to the cavity-tissue interface and finally crosses the cavity region to reach the endoscopic detector. Thus, the hybrid light transport model was designed to include two parts; one to describe the light propagation in tissues, and the other to illustrate the light propagation from the cavity-tissue interface to the detector. Assuming that there is a good compromise between the model

This manuscript was accepted by J. Appl. Phys. Click here to see the version of record.

accuracy and the computational time, we employed hybrid simplified spherical harmonics with diffusion equation (HSDE) to describe the luminescent light propagation in tissues. The concise form of the HSDE can be expressed as:[26]

$$\begin{aligned}-\nabla\cdot C_{k,\nabla\Phi_1}(\vec{r})\nabla\Phi_1(\vec{r})-\nabla\cdot C_{k,\nabla\Phi_2}(\vec{r})\nabla\Phi_2(\vec{r})+\\ C_{k,\Phi_1}(\vec{r})\Phi_1(\vec{r})+C_{k,\Phi_2}(\vec{r})\Phi_2(\vec{r})=C_{k,S}(\vec{r})S(\vec{r}) \quad \vec{r}\in\Omega.\end{aligned} \tag{1}$$

Here, $\Phi_k(\vec{r})(k=1,2)$ is the moment of composite areas that is related to the nodal flux density at node $\vec{r}$; $S(\vec{r})$ is the light source (radioactive tracer or RLNP); Ω denotes the domain that the tissues occupied; $C_{k,\nabla\Phi_1}(\vec{r})$, $C_{k,\nabla\Phi_2}(\vec{r})$, $C_{k,\Phi_1}(\vec{r})$, $C_{k,\Phi_2}(\vec{r})$, and $C_{k,S}(\vec{r})(k=1,2)$ describe the tissues' optical properties and boundary related parameters.[26]

The exiting partial current at the cavity-tissue interface can be calculated by:[26]

$$J(\vec{r})=\left|\beta_1(\vec{r})\Phi_1(\vec{r})+\beta_2(\vec{r})\Phi_2(\vec{r})\right|, \quad \vec{r}\in B, \tag{2}$$

where $\beta_k(\vec{r})(k=1,2)$ is a boundary related parameter of a point $\vec{r}$ at the cavity-tissue interface B.

During endoscopic detection, an imaging balloon catheter is required to be inserted and filled with air to hold up an organ cavity when collecting luminescence.[27] Taking into consideration the aperture angle of the collecting lens used in the endoscopic detector,[21] the light power P collected on the endoscopic detector can be calculated as follows:

$$P(\vec{r}_d)=\int_B J(\vec{r})\theta(\vec{r},\vec{r}_d)T(\vec{r},\vec{r}_d)dB, \quad \vec{r}\in B,\vec{r}_d\in R. \tag{3}$$

Here, R is the detection domain of the endoscopic detector; $\vec{r}_d$ denotes one detection pixel at the detector; θ is the aperture angle function used to determine whether the luminescence can be collected by the endoscopic detector;[21] T denotes a system response function that describes the luminescence propagating from the cavity-tissue interface B to the detector R:

$$T(\vec{r},\vec{r}_d)=\tau\frac{\cos\alpha_{\vec{r}}\cos\alpha_{\vec{r}_d}}{\left|\vec{r}_d-\vec{r}\right|^2}e^{-\mu_a'\left|\vec{r}_d-\vec{r}\right|}, \quad \vec{r}\in B,\vec{r}_d\in R, \tag{4}$$

This manuscript was accepted by J. Appl. Phys. Click here to see the version of record.

where τ denotes the attenuation rate of the imaging balloon catheter; $\alpha_{\vec{r}}$ and $\alpha_{\vec{r}_d}$ are the angles between the vector of $\left|\vec{r}_d - \vec{r}\right|$ and the surface normal at $\vec{r}$ and $\vec{r}_d$ respectively; μ_a' is the absorption coefficient of the cavity region.

Incorporating the modeling of the luminescent light propagation in tissues and the cavity region, the mathematically forward model of the endoscopic CLT or RLT geometry can be summarized as:

$$\begin{cases} -\nabla \cdot C_{k,\nabla\Phi_1}(\vec{r})\nabla\Phi_1(\vec{r}) - \nabla \cdot C_{k,\nabla\Phi_2}(\vec{r})\nabla\Phi_2(\vec{r}) + \\ \quad C_{k,\Phi_1}(\vec{r})\Phi_1(\vec{r}) + C_{k,\Phi_2}(\vec{r})\Phi_2(\vec{r}) = C_{k,S}(\vec{r})S(\vec{r}), \quad \vec{r} \in \Omega \\ P(\vec{r}_d) = \int_B \left(\begin{array}{l} \left(\beta_1(\vec{r})\Phi_1(\vec{r}) + \beta_2(\vec{r})\Phi_2(\vec{r})\right) \\ \theta(\vec{r}, \vec{r}_d)\tau \dfrac{\cos\alpha_{\vec{r}} \cos\alpha_{\vec{r}_d}}{\left|\vec{r}_d - \vec{r}\right|^2} e^{-\mu_a'\left|\vec{r}_d - \vec{r}\right|} \end{array} \right) dB, \quad \vec{r} \in B, \vec{r}_d \in R \end{cases} \tag{5}$$

Using the finite element discretization, we can convert Eq. (5) into a linear matrix equation that describes the relationship between the expected distribution of the light source and the measured light power by the endoscopic detector:

$$\Xi S = P. \tag{6}$$

Here, $\Xi = \Sigma A$ denotes the system matrix for the endoscopic CLT or RLT problem. The matrix A has the same form as that published in a previous work,[26] and the elements of the matrix Σ can be defined as:

$$\Sigma_{ij} = \theta(\vec{r}_j, \vec{r}_{di})T(\vec{r}_j, \vec{r}_{di})\Delta S_i \Delta S_j. \tag{7}$$

Here, ΔS_i and ΔS_j indicate the cellar area at points $\vec{r}$ and $\vec{r}_d$ respectively.

Since the measurements collected by an endoscopic detector are severely insufficient, Eq. (6) is extremely ill-posed and hard to solve directly. Taking into consideration the sparse distribution of the light source, the solution to Eq. (6) can be converted into solving the following l_1-norm-based regularization problem:

This manuscript was accepted by J. Appl. Phys. Click here to see the version of record.

$$\hat{S} = \arg\min_{S>0} \frac{1}{2}\left\|\Xi S - P\right\|_2^2 + \tau\left|S\right|_1, \quad (8)$$

where τ is the regularization parameter. Here, Eq. (8) is solved by the primal-dual interior-point algorithm.[28]

3. Experiments and Results

Table I Geometrical parameters of each object in the phantom (units in cm)

Tissues	Shape	Center	Half length
T_1	Cylinder	(0, 0, 0)	(10, 10, 10)
T_2	Ellipsoid	(-7, 0, 0)	(2, 5, 5)
T_3	Ellipsoid	(0, -7, 0)	(5, 2, 2)
T_4	Ellipsoid	(0, 2, 0)	(4, 3, 3)
T_5	Ellipsoid	(0, -3, 0)	(2.5, 1.5, 1.5)
T_6	Cylinder	(0, 7.5, 0)	(1.5, 1.5, 7.5)
T_7	Ellipsoid	(7, 0, 0)	(2, 5, 5)

The feasibility of the proposed endoscopic CLT and endoscopic RLT geometry model was verified with a heterogeneous phantom based simulation. The dimension of the phantom was 10 cm in radius and 20 cm in height, and consisted of six objects with different shapes and sizes to simulate heterogeneity (Table I and Fig. 3). The optical properties of the phantom are listed in Table II.[24] A solid sphere of 1 cm in diameter was positioned at the origin to mimic the luminescence emission source. The endoscopic detector acquired luminescence at 550 and 650 nm. An endoscopic detector that was comprised of an array with a diameter of 1 cm and a center at (0, -3, 0) cm, was longitudinally moved between the heights of -0.5 to 0.5 cm along the z axis with a step size of 0.05 cm. The aperture angle of the detector was set as 120^{o}. The volume power densities of the luminescence emission sources were set to be 0.995 $\mu W/cm^3$ at 550nm, and 0.398 $\mu W/cm^3$ at 650nm respectively, which is consistent with the distribution of the CL spectrum.[29] For comparisons, the DA and SP_3 model based geometries were

This manuscript was accepted by J. Appl. Phys. Click here to see the version of record.

employed as the references. We calculated the localization error (LE) and quantification error (QE) to evaluate the results quantitatively. The LE is calculated by the distance between the maximum density position of the reconstructed source and the central position of the actual one. The QE is the relative error of the reconstructed volume power density compared with the actual value.

Table II Optical properties of each object in the phantom (units in mm^{-1}).

Tissues	550 nm		650 nm	
	μ_a	μ_s'	μ_a	μ_s'
T_1	0.0889	1.3409	0.0050	1.2273
T_2	4.1657	2.4136	0.2630	2.2091
T_3	1.5240	3.0352	0.0881	2.3585
T_4	1.3608	1.2782	0.0786	1.0066
T_5	0	0	0	0
T_6	1.9245	4.7486	0.1021	2.4144
T_7	4.1657	2.4136	0.2630	2.2091

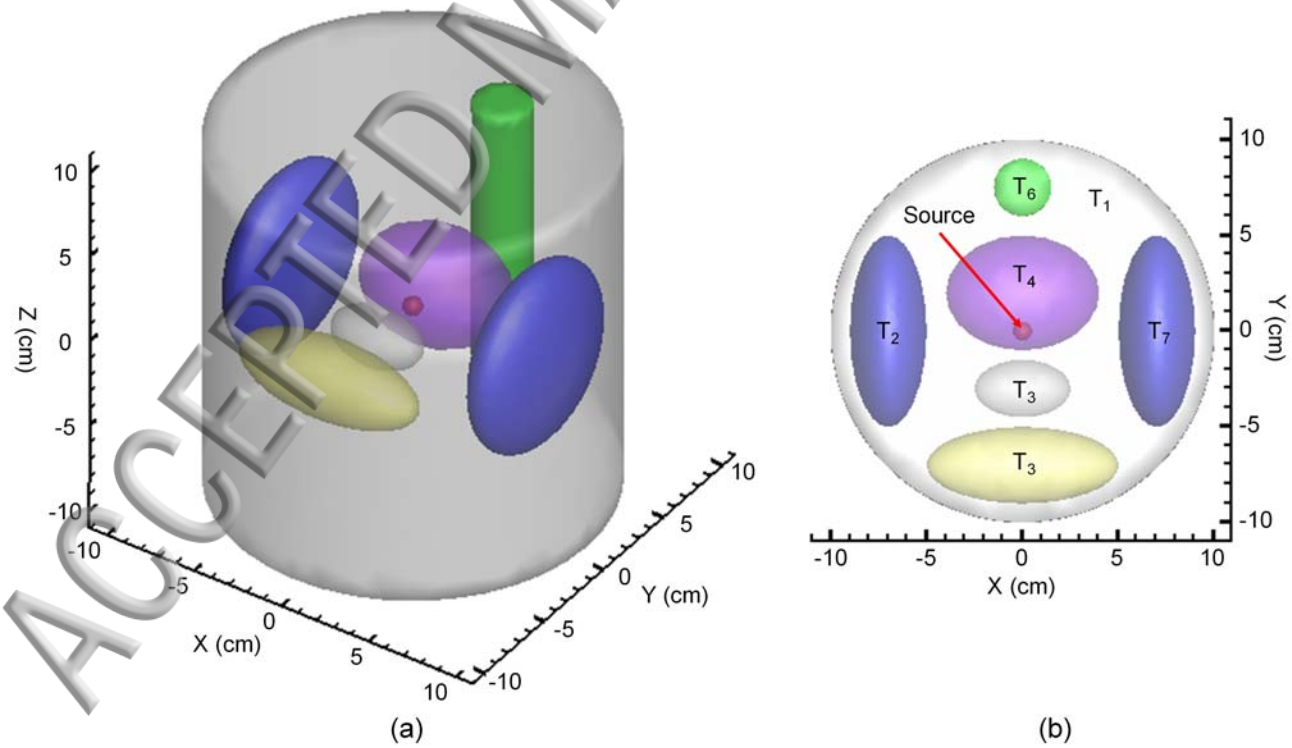

Fig. 3 The dimensions and structures of the phantom used in the simulation. (a) 3D rendering of the geometry; (b) 2D projection from XY view.

This manuscript was accepted by J. Appl. Phys. Click here to see the version of record.

Figure 4 shows the reconstructed results by the proposed model and the DA and the SP_3 based geometries at the wavelength of 650 nm or 550 nm. The related quantitative results are listed in Table III. Our findings demonstrate that the SP_3 based geometry provided the best localization and quantification results. In addition, the proposed geometry model had almost the same performance as the DA based geometry at the wavelength of 650 nm. This is because most of the objects in the phantom belong to high-scattering tissue. In this case, the DA worked well for modeling CL light propagation. Furthermore, at the wavelength of 550 nm, at which the other scattering effect is dominant, the proposed model performed much better than the DA based geometry. Although the proposed geometry performed a little worse than the SP_3 based geometry, its speed was 4 - 8 times faster (Table III). Such increase in ratio is dependent on the wavelength of the collected luminescence. These results collectively demonstrate that the proposed unified scheme could provide promising reconstruction results in terms of both the localization and quantification with a relatively fast speed. This makes the proposed method to be suitable for endoscopic CLT or RLT application.

Table III Quantitative results from the proposed model, and the SP_3 and DA based geometries. Here, time cost refers to the elapsed time of assembling the system matrix. All of the calculations were performed on a personal computer (Inter(R) Core(TM) i7-6700K CPU at 4.0GHz, 32 GB RAM).

	Methods	Reconstructed position (cm)	LE (cm)	Reconstructed density ($\mu W/cm^3$)	QE	Time cost (s)
650 nm	Proposed	(-0.35, 0.58, 0.26)	0.73	0.367	7.8%	18.92
	SP_3 geometry	(-0.38, 0.33, -0.10)	0.51	0.414	4.0%	159.69
	DE geometry	(-0.35, 0.58, 0.26)	0.73	0.432	8.5%	12.16
550 nm	Proposed	(0.24, -0.22, -0.70)	0.77	1.078	8.3%	40.90
	SP_3 geometry	(-0.38, 0.33, -0.10)	0.51	1.037	4.2%	160.14
	DE geometry	(-0.96, 0.19, 0.66)	1.18	1.595	60%	11.75

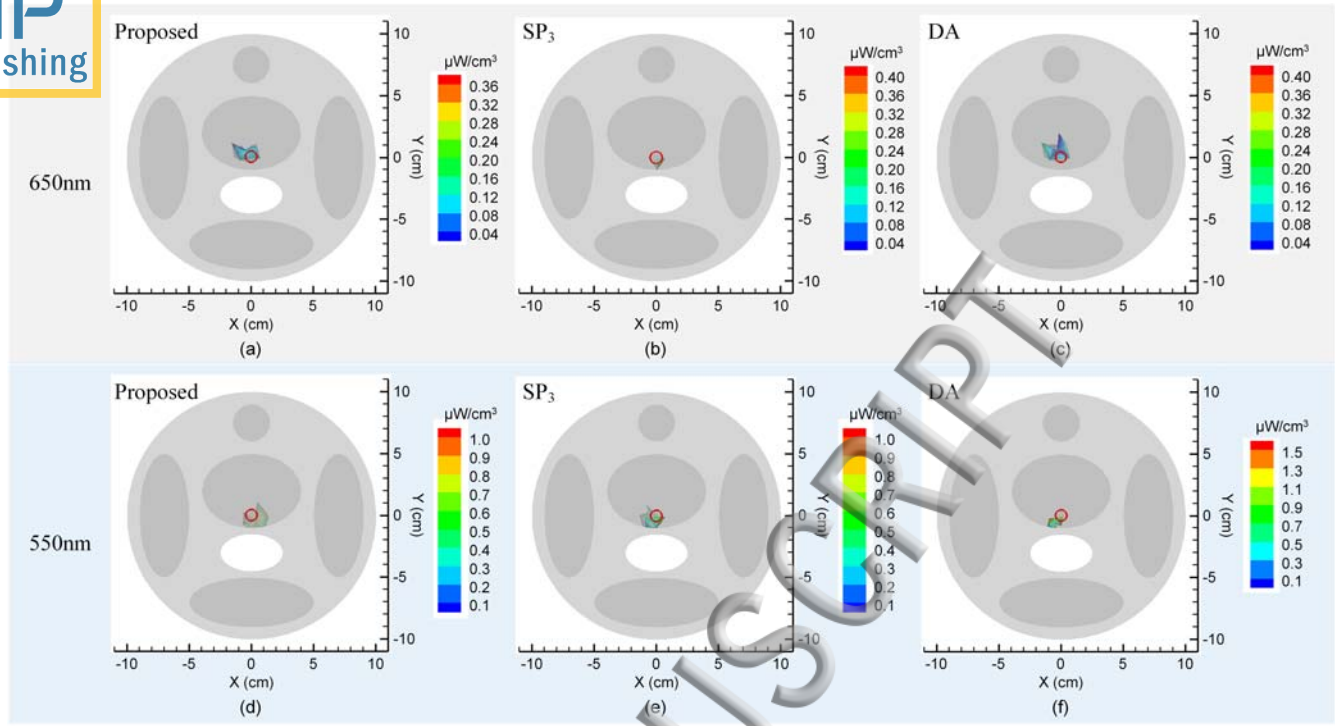

Fig. 4 Reconstructed XY sectional images obtained by the proposed model, SP_3, and DA based endoscopic CLT geometries. (a)-(c) Reconstructed results for the measurements at the wavelength of 650 nm; (d)-(f) at the wavelength of 550 nm; (a) and (d) results reconstructed by the proposed endoscopic CLT geometry; (b) and (e) results obtained from the SP_3 based endoscopic CLT geometry; (c) and (f) from DA based endoscopic CLT geometry.

4. Conclusion

In this study a hybrid-light-transport-model-based unified scheme was proposed for the diversification of tissue optical properties caused by the wide spectra of the Cerenkov/Radio-luminescence. By constructing a more promising mathematical model that combines the SP_3, DA and radiosity equations, we can cater for a wide range of optical properties by providing both the acceptable accuracy and promising speed. The advantage of the model was demonstrated with the heterogeneous phantom based simulation. We believe that the proposed unified scheme will be suitable for endoscopic CLT and RLT applications, especially for the hyperspectral endoscopic CLT and RLT. Prospective studies will focus on the development of the hyperspectral endoscopic CLT and RLT geometry model, and its application to imaging physical phantom and large animals.

Acknowledgments

This work was partly supported by the National Natural Science Foundation of China under Grant Nos. 81627807, 81571725, 61372046, 61401264, 11571012, 61640418, 61701403, the Fok Ying-Tong Education Foundation of China under Grand No. 161104, the Research Fund for Young Star of Science and Technology in Shaanxi Province under Grand No. 2017SR5029, and the Fundamental Research Funds for the Central Universities.

References

1. R. Robertson, M. Germanos, C. Li, G. Mitchell, S.R. Cherry, and M. Silva, Phys. Med. Biol. **54**, N355 (2009).
2. Y. Xu, H. Liu, and Z. Cheng, J. Nucl. Med. **52**, 2009 (2011).
3. T. Shaffer, C. Drain, and J. Grimm, J. Nucl. Med. **57**, 1161 (2016).
4. J. D'Souza, H. Hensley, M. Doss, C. Beigarten, M. Torgov, T. Olafsen, J. Yu, and M. Robinson, J. Nucl. Med. **58**, 175 (2017).
5. A.E. Spinelli, M. Ferdeghini, C. Cavedon, E. Zivelonghi, R. Calandrino, A. Fenzi, A. Sbarbati, and F. Boschi, J. Biomed. Opt. **18**, 020502 (2013).
6. D. Thorek, C. Riedl, and J. Grimm, J. Nucl. Med. **55**, 95 (2014).
7. M.R. Grootendorst, M. Cariati, S.E. Pinder, A. Kothari, M. Douek, T. Kovacs, H. Hamed, A. Pawa, F. Nimmo, J. Owen, V. Ramalingam, S. Sethi, S. Mistry, K. Vyas, D.S. Tuch, A. Britten, M. Van Hemelrijck, G. Cook, C. Sibley-Allen, S. Allen, and A. Purushotham, J. Nucl. Med. **58**, 891 (2017).
8. H. Liu, C. Carpenter, H. Jiang, G. Pratx, C. Sun, M. Buchin, S. Gambhir, L. Xing, and Z. Cheng, J. Nucl. Med. **53**, 1579 (2012).
9. X. Cao, X. Chen, F. Kang, Y. Lin, M. Liu, H. Hu, Y. Nie, K. Wu, J. Wang, J. Liang, and J. Tian, Biomed. Opt. Express **5**, 3660 (2014).
10. T. Song, X. Liu, Y. Qu, H. Liu, C. Bao, C. Leng, Z. Hu, K. Wang, and J. Tian, Mol. Imaging **14**, 443 (2015).
11. H. Hu, X. Cao, F. Kang, M. Wang, Y. Lin, M. Liu, S. Li, L. Yao, J. Liang, J. Liang, Y. Nie, X. Chen, J. Wang, and K. Wu, Eur. Radiol. **25**, 1814 (2015).
12. A. Glaser, R. Zhang, S. Davis, D. Gladstone, and B. Pogue, Opt. Lett. **37**, 1193-1195 (2012).
13. R. Zhang, D. Gladstone, L.A. Jarvis, R. Strawbridge, P. Hoopes, O. Friedman, A. Glaser, and B. Pogue, J. Biomed. Opt. **18**, 110504 (2013).
14. X. Ma, F. Kang, F. Xu, A. Feng, Y. Zhao, T. Lu, W. Yang, Z. Wang, M. Lin, and J. Wang, PLoS ONE **8**, e77926 (2013).
15. X. Cao, X. Chen, F. Kang, Y. Zhan, X. Cao, J. Wang, J. Liang, and J. Tian, ACS Appl. Mater. Interfaces **106**, 213702 (2015).
16. Z. Hu, Y. Qu, K. Wang, X. Zhang, J. Zha, T. Song, C. Bao, H. Liu, Z. Wang, J. Wang, Z. Liu, H. Liu, and J. Tian, Nat. Commun. **6**, 7560 (2015).
17. T.M. Shaffer, E.C. Pratt, and J. Grimm, Nat. Nanotechnol. **12**, 106-117 (2017).
18. X. Cao, X. Chen, F. Kang, X. Cao, Y. Zhan, J. Wang, K. Wu, and J. Liang, Appl. Phys. Lett. **106**, 213702 (2015).
19. D. Piao, H. Xie, W. Zhang, J. Krasinski, G. Zhang, H. Dehghani, and B.W. Pogue, Opt. Lett. **31**, 2876 (2006).
20. X. Chen, J. Liang, H, Zha, X. Qu, D. Chen, Q. Zhang, X. Gao, and J. Tian, Appl. Phys. Lett. **99**, 073702 (2011).
21. X. Chen, J. Liang, X. Cao, D. Yang, D. Chen, J. Ripoll, and J. Tian, J. Appl. Phys. **114**, 084701 (2013).
22. H. Zhao, X. Zhou, Y. Fan, and F. Gao, J. X-ray Sci. Technol. **19**, 57 (2011).
23. Z. Qin, S. Cui, H. Zhao, X. Zhou, M. Jia, Y. Yang, Y. Fan, and F. Gao, J. X-ray Sci. Technol. **21**, 527 (2013).
24. G. Alexandrakis, F. Rannou, and A.F. Chatziioannou, Phys. Med. Biol. **50**, 4225 (2005).
25. A. Gibson, J. Hebden, and S. Arridge, Phys. Med. Biol. **50**, R1 (2005).
26. X. Chen, F. Sun, D. Yang, S. Ren, Q. Zhang, and J. Liang, Phys. Med. Biol. **60**, 6305 (2015).
27. H.L. Fu, Y. Leng, M. Cobb, K. Hsu, J. Hwang, and X. Li, J. Biomed. Opt. **13**, 060502 (2008).

28. Q. Zhang, H. Zhao, D. Chen, X. Qu, X. Chen, X. He, W. Li, Z. Hu, J. Liu, J. Liang, and J. Tian, Opt. Commun. **284**, 5871 (2011).
29. H. Guo, X. He, M. Liu, Z. Zhang, Z. Hu, and J. Tian, IEEE Trans. Med. Imaging **36**, 1337 (2017).

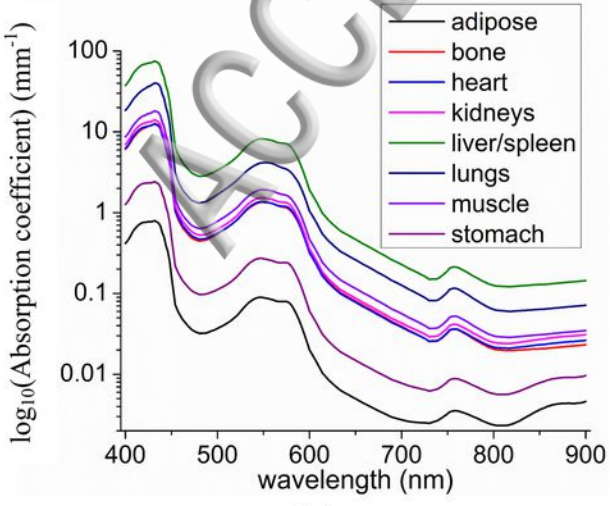
adipose
bone
heart
kidneys
liver/spleen
lungs
muscle
stomach
log10(Absorption coefficient) (mm-1)
wavelength (nm)
100
10
1
0.1
0.01
400
500
600
700
800
900

(a)

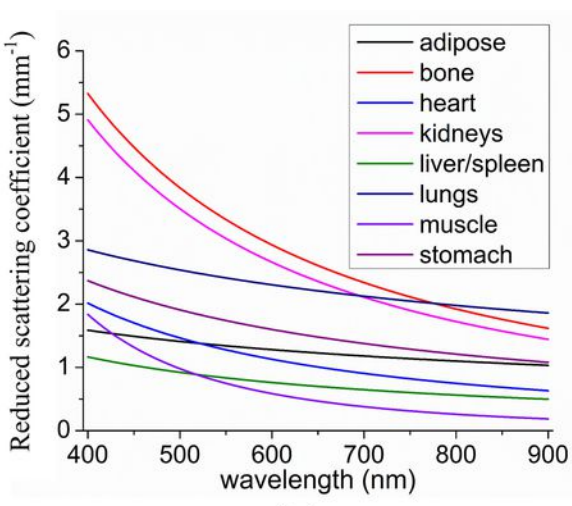
adipose
bone
heart
kidneys
liver/spleen
lungs
muscle
stomach
Reduced scattering coefficient (mm-1)
wavelength (nm)
6
5
4
3
2
1
0
400
500
600
700
800
900

(b)

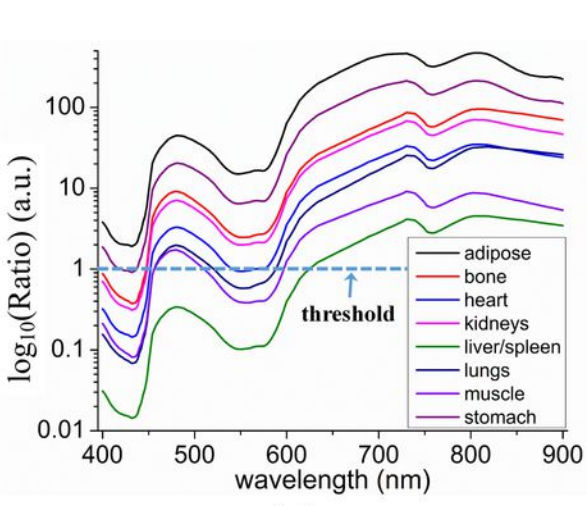
log10(Ratio) (a.u.)
threshold
adipose
bone
heart
kidneys
liver/spleen
lungs
muscle
stomach
wavelength (nm)
100
10
1
0.1
0.01
400
500
600
700
800
900

(c)

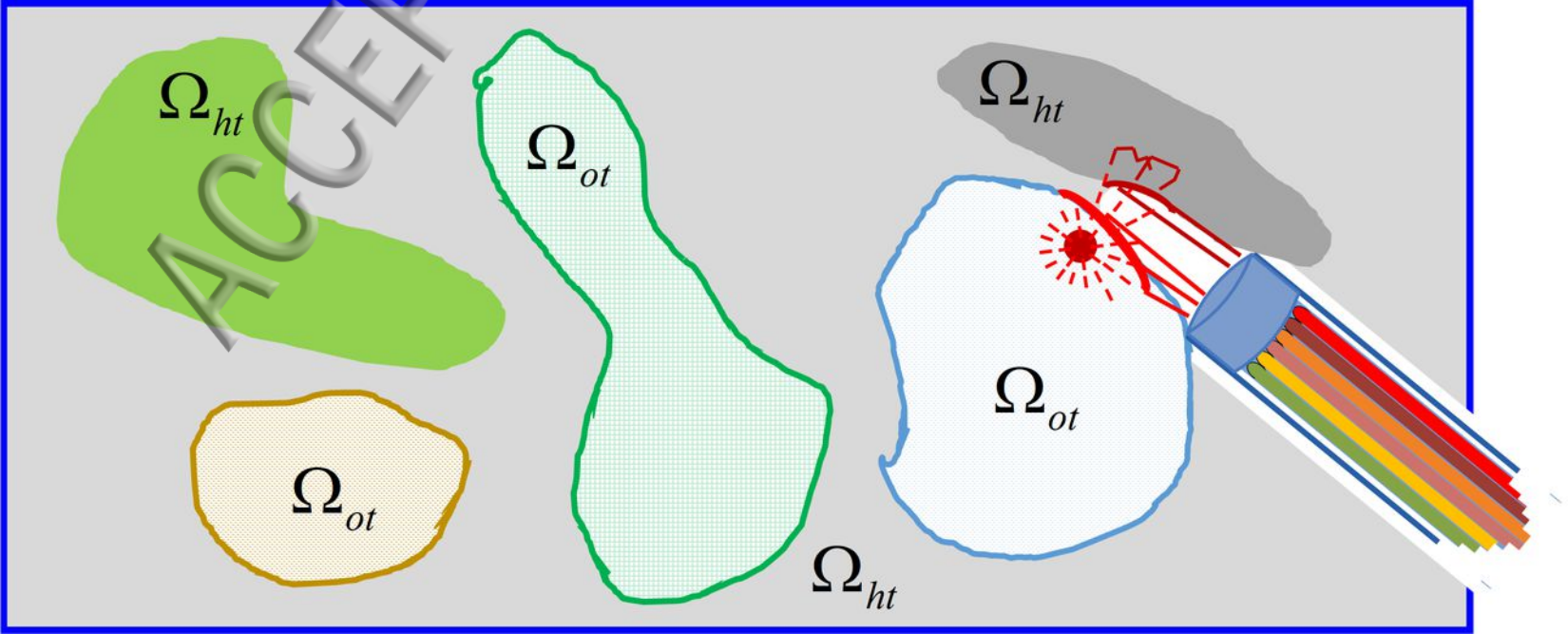
Ω_{ht}
Ω_{ot}
Ω_{ot}
Ω_{ht}
Ω_{ht}
Ω_{ot}

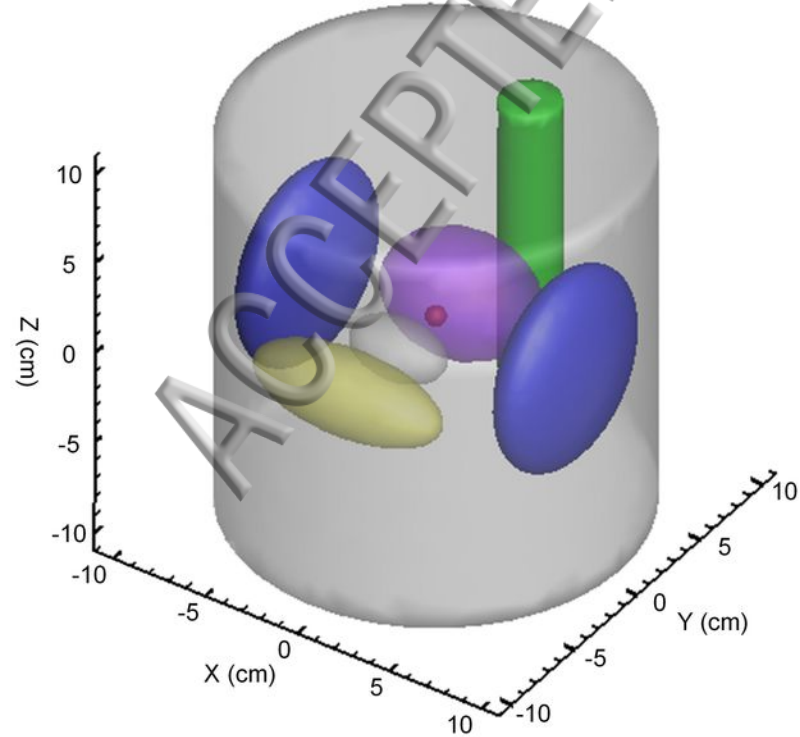
10
5
0
-5
-10
Z (cm)
-10
-5
0
5
10
X (cm)
10
5
0
-5
-10
Y (cm)

(a)

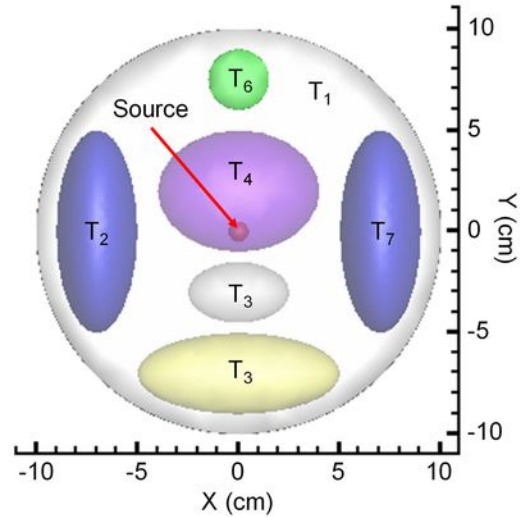
Source
T6
T1
T4
T2
T7
T3
T3
10
5
0
-5
-10
Y (cm)
-10
-5
0
5
10
X (cm)

(b)

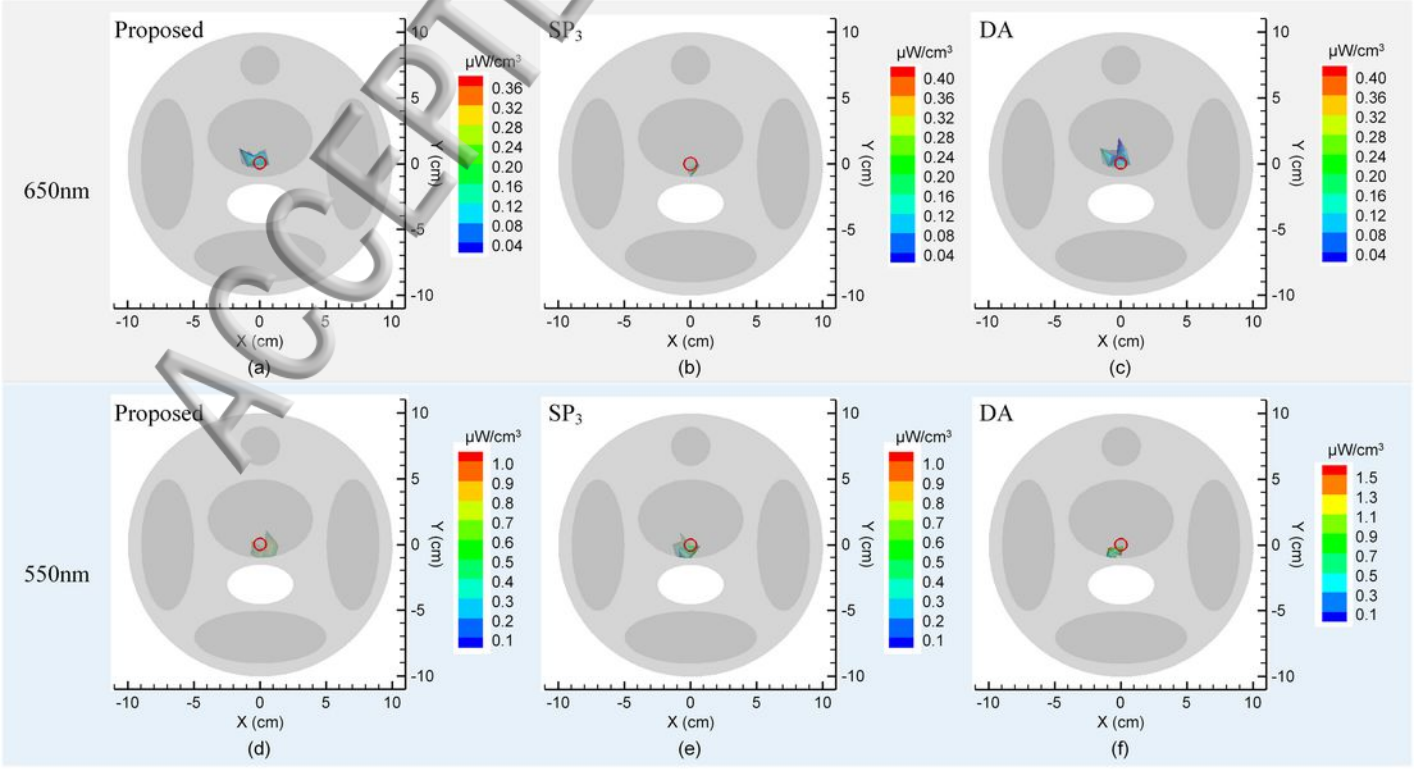
650nm
550nm
Proposed
SP3
DA
μW/cm³
X (cm)
Y (cm)
(a)
(b)
(c)
(d)
(e)
(f)